Progress In Electromagnetics Research C, Vol. 124, 81–96, 2022

Development of an IR-UWB Radar System for High-Resolution Through-Wall Imaging

Mohamed Saad[1, *], Abdelmadjid Maali[1], Mohamed S. Azzaz[1], Azzedine Bouaraba[2], and Mustapha Benssalah[3]

Abstract—Through-Wall-Imaging (TWI) radar offers considerable advantages for applications that require safety and security, such as disaster survivor rescue and tracking terrorist activities. In such situations, the use of an impulse UWB radar system is constantly increasing due to its ability to provide precise images of hidden targets in a short period of time. This paper presents a new radar system for through-wall imaging using an impulse-radio ultra-wideband (IR-UWB) signal. The radar system is built using a field-programmable gate array (FPGA) board, an oscilloscope, and Vivaldi antennas. The radar system transmits impulse signals, which have a monocycle shape with a 400-picosecond duration and a 4.6 GHz bandwidth. The FPGA board is used to produce impulse signals that have a short time duration in the sub-nanosecond range in order to expand the bandwidth of the generated signal and make the developed radar capable of providing high-resolution images. The FPGA-based implementation of the IR-UWB generator offers the flexibility to modify the spectrum characteristics of the generated signal. The receiver side of the radar system collects the echoes using the principle of synthetic aperture radar (SAR), and then the time-domain back-projection algorithm is applied to the radar echo to form 2D images. An indoor imaging experiment was carried out with two human targets to investigate the imaging capability of the designed IR-UWB radar. The obtained experimental results demonstrate that this radar has the potential to deliver high-resolution images of multiple human targets and identify their locations.

1. INTRODUCTION

Through-the-wall imaging radar has the ability to image targets located behind opaque material, such as a wall and door. This capability is desirable in many situations that require safety and security, such as rescue missions and tracking terrorist activities [1].

Ultra-wideband (UWB) signals are extensively used in radar systems for through-obstacle-imaging applications such as through-the-wall imaging radar [2], ground penetration radar (GPR) [3], and medical imaging radar [4]. Due to their ability to provide high-resolution images, when a UWB signal is used, the radar tends to achieve centimeter resolution. In addition, UWB signal has better penetration capacity through materials [5]. The most frequently employed UWB signals are: frequency modulated continuous wave (FMCW) signal [6], stepped frequency continuous wave (SFCW) signal [7], and Impulse IR-UWB signal [8]. Typically, the radar systems that employ CW signals have a simple radar architecture and good target detection abilities [9]. However, the processing time of these radar systems is relatively slow compared to IR-UWB radars for the following reasons. First, IR-UWB radar has the ability to instantly illuminate the scene with a UWB signal, by generating pulses that have an

Received 2 June 2022, Accepted 30 August 2022, Scheduled 16 September 2022

* Corresponding author: Mohamed Saad (saad.mohamed.ts@gmail.com).

[1] Laboratoire Systèmes Électroniques et Numériques, École Militaire Polytechnique, BP 17 Bordj El-Bahri, Algiers, Algeria.

[2] Laboratoire Radar, École Militaire Polytechnique, BP 17 Bordj El-Bahri,Algiers, Algeria. [3] Laboratoire Traitement du Signal, École Militaire Polytechnique, BP 17 Bordj El-Bahri, Algiers, Algeria.

extremely short duration. Second, the reception side of an IR-UWB radar is capable of obtaining a range profile by making a direct acquisition of received echoes. CW radars, on the other hand, need to apply a Fourier transform after each signal acquisition, and the emission side of CW radar requires stepping through a number of frequencies before signal transmission is performed [6, 7, 10]. Indeed, processing time is an important factor in through-wall imaging because, in the practical scenario, the radar system must provide images in the shortest possible time. In this situation, IR-UWB radar is the best choice. However, the design of an IR-UWB radar system for TWI applications is challenging, since the resolution of such a radar depends mainly on the time duration of the generated impulse signal, which should be in the sub-nanosecond time range. Although CMOS technology has been proposed for the design of an IR-UWB generator, this technology suffers from limited UWB bandwidth [11] and design complexity [12].

In recent years, FPGAs have become an essential element in the development phase of many systems that require high performance, fast processing, and high flexibility. FPGAs also represent a promising platform for radar systems because of their ability to implement key radar functions with high efficiency. In the literature, the design of radar systems based on FPGA platforms has been the focus of many studies and research. FPGA board was employed to accelerate the computing speed of radar signal processing [13] and image formation algorithms [14]. In addition, FPGA board was used as an essential component of radar systems. In [15], FPGA boards were integrated into the receiver side of through-the-wall radars in order to acquire a UWB signal. Furthermore, FPGA was used to efficiently realize the generation of radar transmission signals. In [16], an FPGA-based implementation was developed to produce a chirp signal for high-resolution SAR applications. This signal has a bandwidth of 100 MHz and a chirp rate of 5 MHz/s. Another technique, proposed in [17], uses OpenCL approach to generate digital chirp signals on Altera Cyclone V FPGA. In [18], an FPGA Virtex-2 was used to produce IR-UWB impulse signals that had a bandwidth of 41.5 MHz and a center frequency of 110.25 MHz. In [19], a UWB signal generator was implemented using FPGA Virtex-4, which enabled the production of IR-UWB signals that had a bandwidth of 90 MHz and a center frequency of 300 MHz. The authors in [20] previously designed an impulse UWB radar system based on FPGA Virtex-6 for generating Gaussian impulse signals that had a duration of 1-ns and 1 GHz bandwidth. This signal is modulated to 3 GHz via a mixer and a local oscillator. However, the resolution of this radar is low due to the used 1 GHz bandwidth, and the received signal suffers from distortion and noise caused by the use of many components in the construction of this radar. Recently, an IR-UWB radar system has been proposed based on a Xilinx Virtex-6 FPGA board to implement the generation of an IR-UWB Gaussian signal that has a duration of 540 ps and a bandwidth of 2.073 GHz [21]. This radar operates in the frequency band from 117 MHz to 2.19 GHz and is used for the detection of human targets under rubble.

The aim of this work is to design a novel IR-UWB radar system for through-wall imaging. The radar incorporates the generation of an IR-UWB signal using an FPGA Kintex-7 board. To increase the bandwidth of the generated signal, a Gigabit Transceiver (GBT) is used in the FPGA design. The proposed UWB generator produces a monocycle signal, which has a duration of 400 picoseconds and a bandwidth of 4.6 GHz (0.7–5.4 GHz). The FPGA-based implementation of this generator provides flexibility to change the signal bandwidth to address other UWB radar applications. The radar receiving side uses a similar concept to the SAR radar to form 2D images. In fact, this technique increases data collection time due to the need to change antenna locations. Here, the FPGA board controls the receiving antennas using a controlled switch to speed up the SAR operation and make it automatic. Then, the backprojection algorithm is applied to reconstruct the 2D images of the scene behind the wall. Thus, the proposed radar system in this paper offers the following advantages and contributions:

- Development of a radar system has the potential to deliver high-resolution images.
- Propose a new UWB signal generator using the FPGA card to generate radar transmission signals with a bandwidth of 4.6 GHz from 0.7 to 5.4 GHz and centered at 3 GHz.
- Simplify the radar structure by using the monocycle shape of the transmission signal, due to the spectrum of this signal, which is located in higher frequency bands.
- Utilization of a technique allows the automatic collection of radar echoes according to the SAR radar concept by means of an FPGA board.

The remainder of this paper is organized as follows. Section 2 presents the principle of through-the-wall imaging radar using an IR-UWB signal, including the imaging technique used. Section 3 shows the

FPGA implementation of the proposed IR-UWB signal generator. Section 4 presents the experimental setup of the developed radar structure, including the radar specifications. Finally, the experimental results are presented and discussed in Section 5. Section 6 compares the developed radar system in this study with recent similar works.

2. THOUGH-WALL IMAGING USING IR-UWB SIGNAL

This section introduces the principle of through-the-wall imaging using an IR-UWB radar by discussing the mathematical model of the acquired radar echo signal based on the transmission of an IR-UWB signal, and then we show the image reconstruction technique used in this study.

Through-wall imaging radar works by sending radar signals through a wall or other barriers, and "seeing" what is on the other side. The radar signals penetrate through the wall and are then reflected back to the receiving antenna. Next, an adequate imaging algorithm is applied to the reflected signals to reconstruct the images of the scene behind the wall. When an IR-UWB radar is used, the transmission part of the radar system emits a series of N impulse signals at periodic intervals called pulse repetition intervals (PRIs). The radar emission signal can be written as the following equation:

$$S_t(t) = \sum_{n=0}^{N-1} P(t - nT_s) \tag{1}$$

where T_s denotes the PRI, and $P(t)$ is the transmitted impulse signal. The reciprocal of the PRI is called the pulse repetition frequency (PRF). The most common employed impulse waveforms are the Gaussian signal and its first derivative, referred to as the monocycle signal. The Gaussian signal is mathematically represented using Equations (2) [22].

$$P_g(t) = a_0 e^{-\left(\frac{t}{\tau}\right)^2} \tag{2}$$

where a_0 defines the transmission signal amplitude, and τ is the scaling factor to adjust the impulse width. The monocycle signal is given by the following equation.

$$P_m(t) = \frac{2a_0 t}{\tau^2} e^{-\left(\frac{t}{\tau}\right)^2} \tag{3}$$

In this article, the monocycle signal is used as a radar transmission signal. The spectrum of this signal covers a wide band when the signal duration is reduced. The advantage of the monocycle signal compared to the Gaussian signal is that its spectrum is located directly at a high frequency. Figure 1 plots the Gaussian and monocycle waveforms in the time and frequency domain.

The spectrum of the monocycle signal is ultra-wideband similar to the Gaussian signal. However, the monocycle signal has a spectrum located in the higher frequency band, whereas the Gaussian signal has a spectrum centered around the DC component. This spectral characteristic increases the antennas'

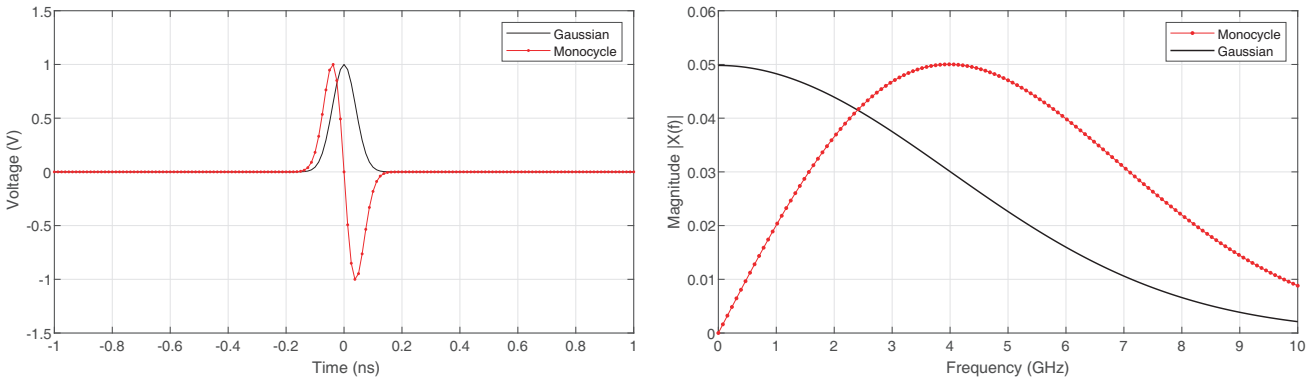

Figure 1. Gaussian and monocycle signals, (a) in the time domain, (b) in the frequency domain.

radiation efficiency and enables the radar system to transmit the monocycle signal directly via antenna without the need for signal modulation [23]. As a result, it allows reducing the components required by the radar architecture, i.e., the mixer and local oscillator.

The duration of a transmission impulse signal is an important parameter that must be considered when the IR-UWB radar system is used because the shorter the duration is, the higher the bandwidth of the signal is, due to the reciprocal relationship between the duration and bandwidth of the transmission signal. Moreover, when a short duration is used, the through-wall imaging radar tends to achieve a higher resolution and can easily distinguish between close targets. Equation (4) defines the relationships between the duration of an impulse signal and the range resolution (ΔR) of a radar imaging system [24].

$$\Delta R = c\frac{\Delta T}{2} \tag{4}$$

where c represents the speed of light, and ΔT is the time-duration of a signal.

The received signal in a through-the-wall imaging scenario, in which a human target is located behind a wall, can be modeled as attenuated and shifted versions of the transmitted signal [25], as illustrated in Equation (5).

$$S_r(t) = \sum_k \alpha_k S_t(t - \tau_k) + n(t) \tag{5}$$

where α_k denotes the reflectivity of k objects in the scene, including both the reflection of the human target and the wall. The term $n(t)$ refers to the noise that is incurred by the UWB channel, and τ_k represents the time delay due to the round-trip propagation delay associated with the location of k objects.

We can see from Equation (5) that the received echo signal changes as a function of object position and reflectivity. In fact, most imaging techniques rely on these two variables to reconstruct through-wall-imaging images.

In essence, through-the-wall imaging radar uses an approach very similar to SAR radar. The concept of a SAR radar is to use a moving platform as an airplane to acquire the echo signal at multiple positions to synthesize a large effective length antenna, which will lead to enhanced imaging resolution [26]. In practice, this operation slows down the system due to the increased time required to collect the echo. To speed up this operation, a switch board is integrated into the radar system to control the functioning of the receiving antennas according to the SAR radar. Figure 2 shows

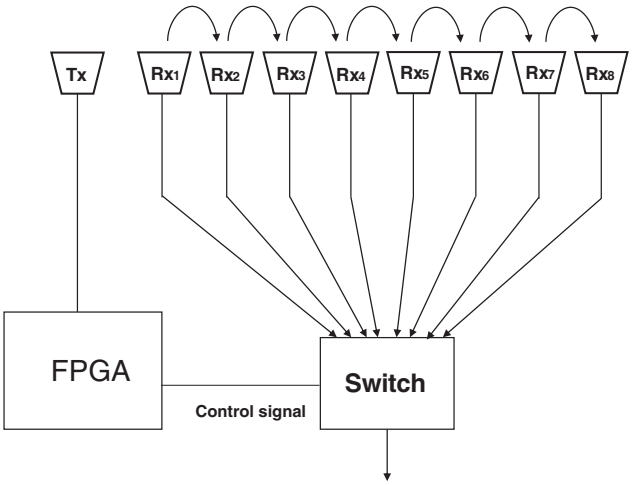

Figure 2. Echo collection using FPGA.

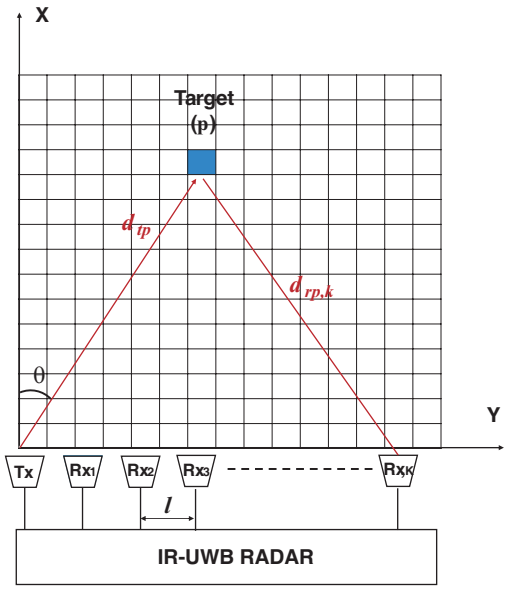

Figure 3. Observation geometry of through the wall imaging radar.

the configuration used for this purpose, which is similar to the configuration of the transmitter-fixed bistatic forward-looking synthetic aperture radar (BFSAR). The switch has one output and eight inputs connected to receiving antennas. The FPGA feeds the switch with a control signal to sequentially select the operating antenna from the first to the eighth. This solution enables the radar to scan the scene very rapidly, which is also suitable for real-time applications because of the significant minimization of the time required to collect radar echoes.

Numerous SAR imaging algorithms are used for through-wall imaging. Among these algorithms, the back-projection algorithm is the simplest and most widely employed SAR imaging method to obtain 2D and 3D images. The goal of the imaging algorithm is to take the data collected by the multiple antenna positions and process it to form an image of the scene. The through-wall model is presented in Figure 3. The back-projection algorithm produces the pixel intensity $\eta(p)$ by coherently adding the echo signal collected by each antenna position as a function of the round-trip delay time $T_{p,k}$, as expressed in the following equation [27].

$$\eta(p) = \sum_{k=1}^{K} S_{r,k}(T_{p,k}) e^{j\frac{2\pi}{c}T_{p,k}F_c} \tag{6}$$

where K represents the total number of the reception antennas, $S_{r,k}$ the signal captured by the k receiving antenna, and F_c the center frequency of the monocycle signal. The term $j\frac{2\pi}{c}T_{p,k}F_c$ is used to compensate for the phase introduced by the carrier frequency [26], and $T_{p,k}$ is the round-trip delay time, which can be expressed by Equation (7):

$$T_{p,k} = \frac{d_{p,k}}{c} \tag{7}$$

where $d_{p,k}$ is the total distance traveled from the transmitting antenna to the target P and back to the k receiving antenna. The distance $d_{p,k}$ has a direct relationship with the round-trip delay time. The adopted image formation method is a geometric approach that forms the images as a function of the round-trip delay time. Hence, calculating the exact distance according to the antennas location is an important parameter that needs to be considered during the image formation stage. The distance $d_{p,k}$ is given by the following relation.

$$d_{p,k} = d_{tp} + d_{rp,k} = d_{tp} + \sqrt{d_{tp} + (k \cdot l)^2 - 2 \cdot d_{tp}(k \cdot l) \cdot \sin\theta} \tag{8}$$

where

- d_{tp} is the distance that separates the P target from the transmitting antenna.
- $d_{rp,k}$ is the distance that separates the P target from the k receiving antenna.
- l is the distance between the antennas.

In the practical scenario of TWI, the wall effect must be considered to compensate for the problem of image defocusing. When the wave passes through the wall, the propagation slows down. The wall has a different dielectric constant from the free space, which leads to the deceleration of the radar signal's propagation speeds and signal refraction. Thus, the existence of a wall will cause an additional delay in the arrival time of the receiving signal compared to the scenario without the wall. The through-wall model in the presence of the wall effect is depicted in Figure 4.

According to [28], the propagation model through the wall can be considered as a two-layer model as depicted in Figure 4. When the radar signal travels from Tx antenna to the target and then back to the k-th receiving antenna, refractions will occur on the air-to-wall and wall-to-air interfaces. P1 and P2 represent the corresponding refraction points. The total electrical length between radar and target is a superposition of a four-segment path, which can be expressed by the following equation [29].

$$L_{tr,k} = L_t + \sqrt{\varepsilon_r} L_{tw} + L_{r,k} + \sqrt{\varepsilon_r} L_{rw,k} \tag{9}$$

where ε_r is the dielectric constant of the wall; $L_t w$ and L_t are the distances from the transmitting antenna to P1 and from P1 to the target, respectively; and $L_{r,k}$ and $L_{rw,k}$ are the distances from the target to P2 and from P2 to the k-th receiving antenna, respectively. Knowledge of the wall parameters,

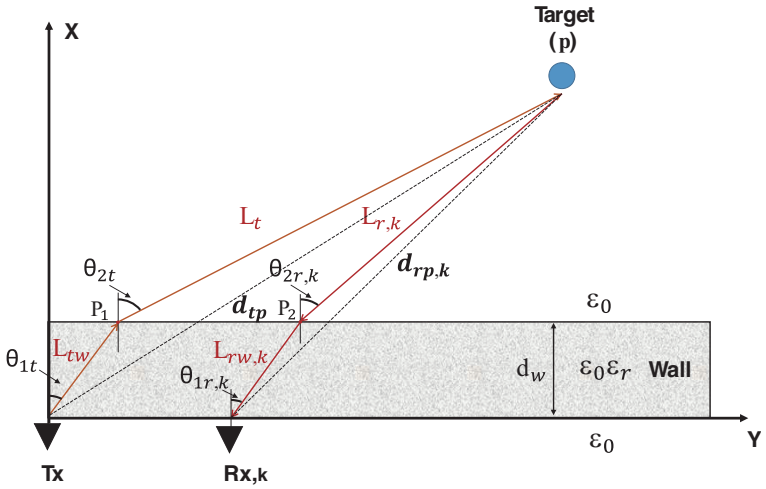

Figure 4. Wave propagation model through-the-wall.

such as dielectric constant and thickness, is necessary for the calculation of the total electrical length. Equation (10) determines the total electrical length as a function of wall parameters [28].

$$L_{tr,k} = d_{p,k} + d_w\left(\sqrt{\varepsilon_r - \sin^2(\theta_{2t})} + \cos(\theta_{2t})\right) + d_w\left(\sqrt{\varepsilon_r - \sin^2(\theta_{2r,k})} + \cos(\theta_{2r,k})\right) \tag{10}$$

d_w is the wall thickness, θ_{2t} the refracted angle on the refraction point P1, and $\theta_{2r,k}$ the incident angle on the refraction point P2. The relationship between the incidence and refraction angle can be determined by applying the Snell-Descartes law as

$$\sin(\theta_{2t}) = \sqrt{\varepsilon_r}\sin(\theta_{1t}) \tag{11}$$

$$\sin(\theta_{2r,k}) = \sqrt{\varepsilon_r}\sin(\theta_{1r,k}) \tag{12}$$

3. FPGA IMPLEMENTATION OF IR-UWB GENERATOR

In this section, we present the hardware implementation of the IR-UWB impulse generator using an FPGA Kintex-7 board. The impulse signal generated by the FPGA has a monocycle form, which presents good properties in terms of signal bandwidth and center frequency. In addition, the FPGA based implementation of this generator provides the flexibility to change the spectral propriety and PRI of the signal according to the requirements.

Figure 5 depicts the overall block diagram of the proposed IR-UWB signal generator implemented in FPGA KC705.

In this design, Xilinx Intellectual Property (IP) cores are used to implement the design blocks. There are three different blocks, including a Gigabit Transceiver (GBT), random access memory (RAM), and a clocking generator based on a mixed-mode clock manager (MMCM).

The GBT architecture is designed to enable the FPGA to transmit and receive data over high-speed serial links with data line rates ranging from 0.5 to 12.5 Gbps [30]. It provides a method for increasing data transfer bandwidth and has the ability to handle a variety of data sizes. In addition, the data can be transferred via 16 interface connections, such as the SMA connector, FMC connector, and PCI connector [31]. In this implementation, the GBT block is configured in (TX) mode to transmit the data stored in block RAM, and the SMA interfaces are chosen as the outputs of this data. To access the GBT transceiver connected to the SMA connector, the channel "GTXE2_CHANNEL_X0Y8" is selected in the IP core configuration parameter. This allows data transmission via the SMA positive signal transmitter (TXP) and SMA negative signal transmitter (TXN) connectors using the low voltage differential signaling (LVDS) standard. Thus, two complementary signals are generated on these outputs (see Figure 6). The time duration T_d of these signals depends on the selected GBT line rate, as written

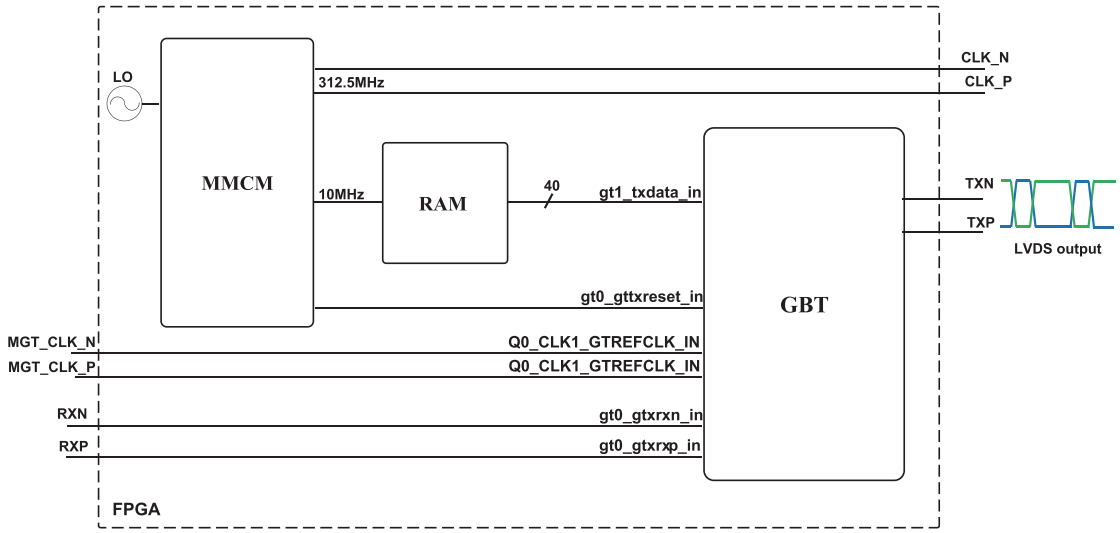

Figure 5. Block diagram of UWB signal generation using GBT core.

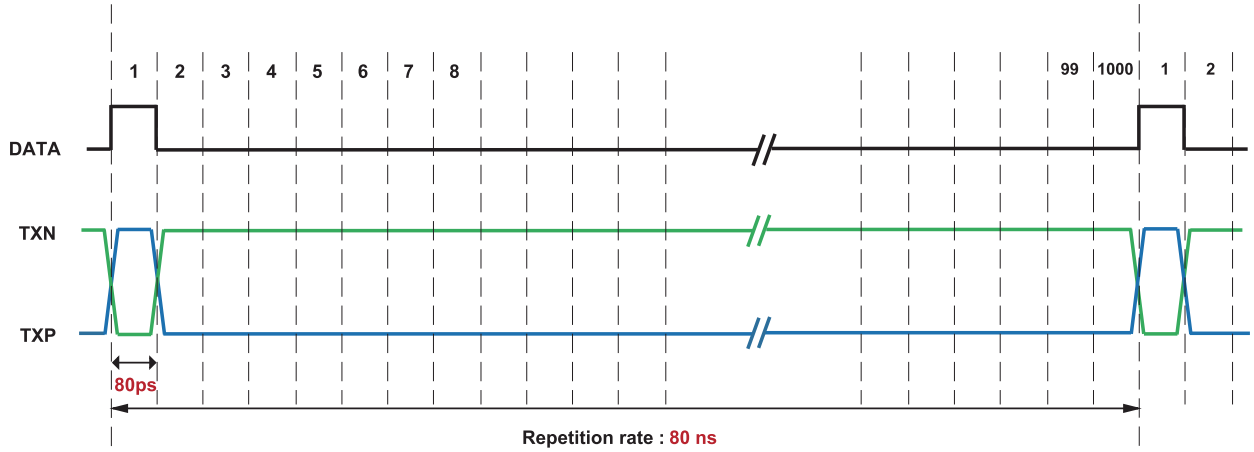

Figure 6. Data bits stored in the RAM and their corresponding GTB outputs.

in the following equation.

$$T_d = \frac{1}{Line\ rate} \tag{13}$$

To obtain a minimum time-duration of 80 ps, the maximum line rate of 12.5 Gbps is chosen.

The GBT clock resources are external through MGT_REFCLK_P and MGT_REFCLK_N. These two inputs supply the GBT reference clocks with the desired clock signals. The clock frequency required by the GBT is determined by the selected GBT line rate and data widths, as shown in Equation (14).

$$F_{REF} = \frac{Line\ Rate}{Data\ Width} \tag{14}$$

The GTB-REF clocks are set to 312.5 MHz, as the line rate and data width of the GBT are set to 12.5 Gb/s and 40 bits, respectively. Both of these clocks are provided by the MMCM IP core. From the internal local oscillator (LO) of the FPGA, the MMCM can output multiple clock signals with different frequencies that match the requirements of the GBT and RAM memory. The MMCM is also used to generate a 10 MHz clock for the memory block to synchronize the write operation to the GTB. The block memory was created based on the single-port RAM mode, which allows writing the data bits $\{1; 0\}$ to the GBT. The memory width and depth parameters are set to 40 and 25, respectively,

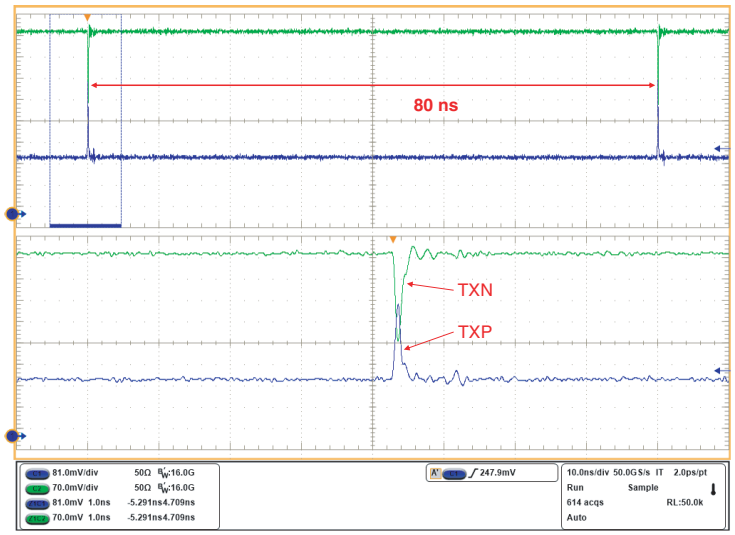

Figure 7. Signals generated at GBT outputs.

to transfer the data bits in 40-bit parts. In addition, the RAM is initialized using a COE file. This file contains 1000 bits, where the first bit is "1" and the rest is "0", to set the repetition rate of the generated signal to 80 ns (Figure 6).

Figure 7 depicts the output signals at the TXP and TXN ports captured with a 100 Gsps sampling oscilloscope. The upper part of this figure shows the repetition rate of the generated signal. The spacing used between the "1" bits sets the time interval between the generated signal to 80 ns. This time represents the radar pulse repetition interval, which makes the radar system transmit the generated signal every 80 ns. The lower part of the Figure 7 represents the shape of the generated signal, which consists of two complementary Gaussian signals. A Gaussian signal is generated at the TXP port and its opposite signal at the TXN port. Due to the high transmission rate of GBT, these signals have an extremely short duration.

To generate the monocycle signal, these two Gaussian signals are combined after introducing a delay at the TXN output. The TXN signal is delayed by 200 ps, and then this signal is combined with the TXP signal by means of a ZX10-2-183-S+ power combiner.

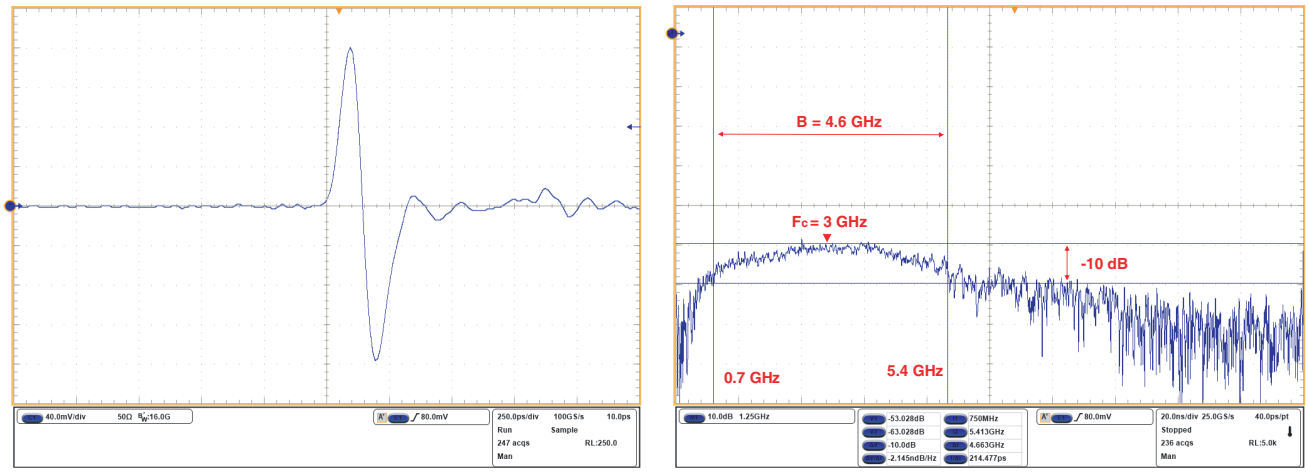

(a) (b)

Figure 8. Resulted monocycle signal for GBT line rate 12.5 Gb/s, (a) in the time domain, (b) in the frequency domain.

The resulting signal obtained after the combination stage is shown in Figure 8(a), which is a monocycle waveform having the following properties: a duration about 400 ps, 320 mv (peak to-peak), symmetry between the positive and negative parts, and a small ringing level. The corresponding spectrum of this signal is given in Figure 8(b), which has a bandwidth of 4,6 GHz from 0.7 to 5.4 GHz, and is centered at 3 GHz.

It is important to note that the proposed IR-UWB generator provides the flexibility to change the monocycle duration through changing the GBT line rate. Accordingly, the spectrum and center frequency of this signal will change. Figure 9(a) shows the resulting monocycle signal for the GTB line rate of 4 Gb/s. This signal has a duration about 600 ps and a bandwidth of 1.5 GHz (0.5 to 2 GHz) centered at 1.25 GHz (see Figure 9(b)). The bandwidth of the new signal is reduced approximately by three times when the GBT line rate is deceased by three times.

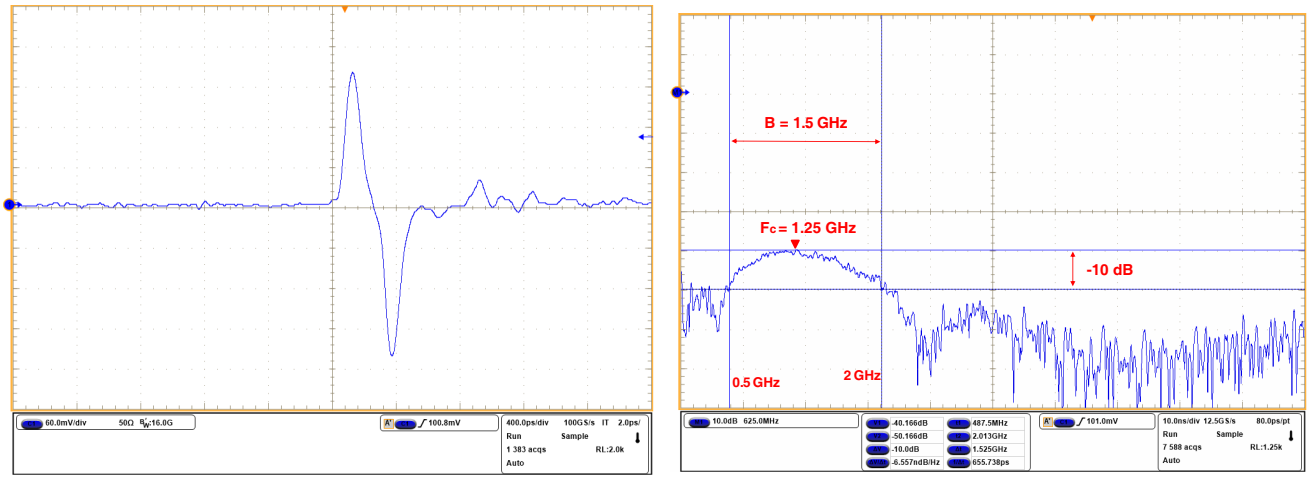

(a) (b)

Figure 9. Resulted monocycle signal for GBT line rate of 4 Gb/s, (a) in the time domain, (b) in the frequency domain.

4. DESIGNED IR-UWB RADAR FOR THROUGH-WALL IMAGING

The designed IR-UWB radar system consists of an FPGA, an oscilloscope, UWB components, antennas, and a computer. The FPGA board is responsible for two main tasks of the radar system. First, the FPGA implements the generation of radar transmission signals. This signal has a monocycle shape with an extremely short time duration of 400 ps, resulting in a bandwidth of 4.6 GHz (0.7 to 5.4 GHz). According to Equation (4), the presented IR-UWB radar system achieves a 6-centimeter resolution. The second task of the FPGA is to control the collection process of radar echo. As mentioned in the previous section, the radar imaging system uses a switch board (HMC321ALP4E) controlled by FPGA in order to accelerate the collection process according to the SAR concept. The switch has one output and eight inputs connected to receiving antennas. Figure 10 shows the simulation of the switch control process using the transistor-transistor logic (TTL) signal.

The FPGA feeds the switch with three TTL signals to sequentially select the operating antenna. For this reason, the TTL signals are incremented from "000" to "111" to activate the radar antennas from the first to the eighth. Figure 11 shows the antennas configuration employed in our radar structure.

The antenna design is based on previous efforts to develop a UWB modified Vivaldi antenna for through-obstacle imaging applications [32]. This Vivaldi antenna is utilized due to its advantageous characteristics, which include a simple structure, a directional radiation pattern, a constant gain, and an extremely low mutual coupling effect. The Vivaldi antenna has a constant gain of 8 dB and covers a wide bandwidth.

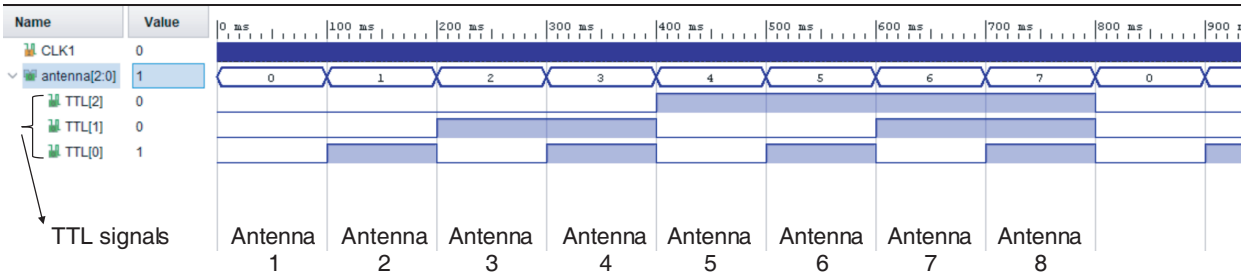

Figure 10. Simulation of switch control operation.

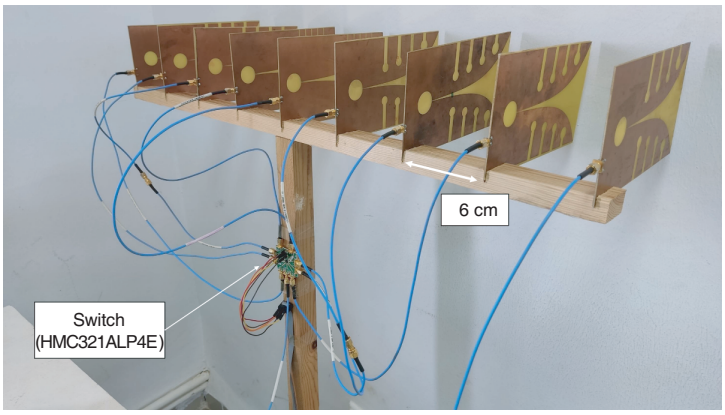

Figure 11. Antennas configuration.

Figure 12 illustrates the detailed block diagram of the designed radar. The TWI radar design consists of a transmitting and a receiving part. On the transmission side, the FPGA generates two complementary Gaussian signals at TXP and TXN. Then, from these outputs, a monocycle waveform is produced by a delay and a power combiner (ZX10-2-183-S+). This signal is then passed through a 30 dB amplification stage via a power amplifier (ZVA-183G-S+) and then sent through a UWB Vivaldi antenna.

On the receiving side, the reflected echo signals are collected using eight receiving antennas. As mentioned in this section, the FPGA controls the echo collection. This is done by controlling the RF switch that is connected to the receiving antennas, by feeding it with a 3-TTL signal to control the selection of the active receiving antenna. The signal from the selected antenna passes through another amplification stage via a power amplifier (ZHL-42W+) and is then captured using a high-sampling oscilloscope (DPO 71604C) to convert the return signal into digital data. The sampling rate of the used oscilloscope is 100 Gsps, with a bandwidth of 16 GHz. The data samples are simultaneously transferred to a PC via an Ethernet link for signal processing and image formation.

5. EXPERIMENTAL IMAGING RESULTS

In complex situations of through-wall imaging, the IR-UWB radar system offers higher precision, and it is more suitable than other UWB radars, due to the simplicity of performing most signal processing methods directly in the time domain [33], which significantly improves the detection sensitivity and accuracy. Typically, the proportion of target reflections in radar returned signals is weak and submerged in the noise, resulting from the wall attenuation and the various stages through which the radar signal passes. To overcome this problem, a signal averaging step is performed by taking the average of 10 successive PRIs. Figure 13 presents the received signal before and after the signal averaging step, where a single human target is located behind the wall.

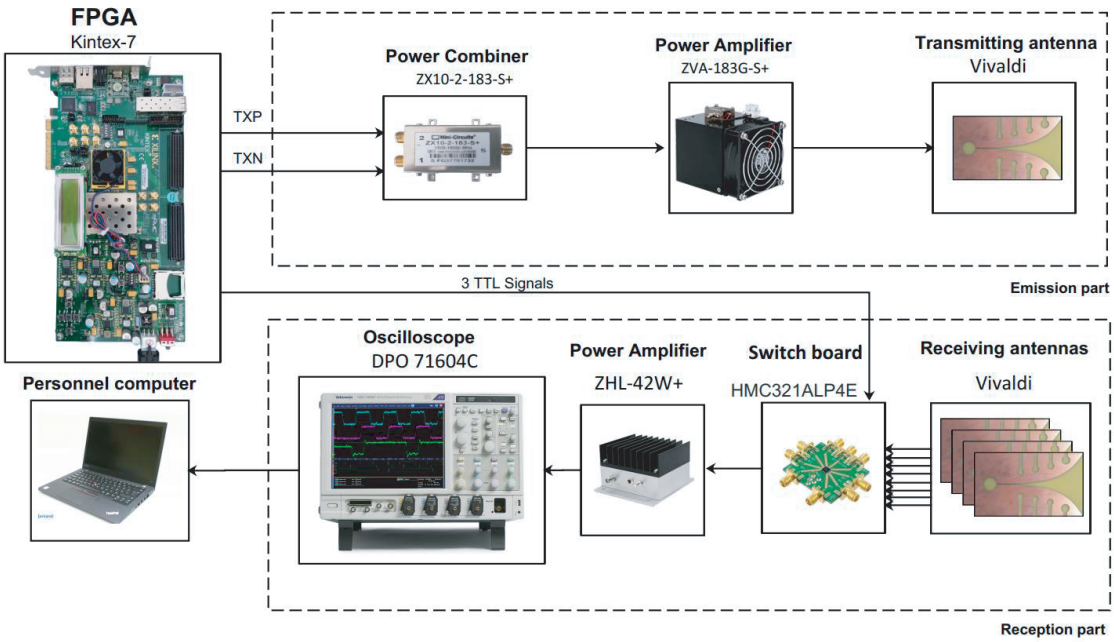

Figure 12. Detailed block diagram of the proposed IR-UWB radar system for TWI.

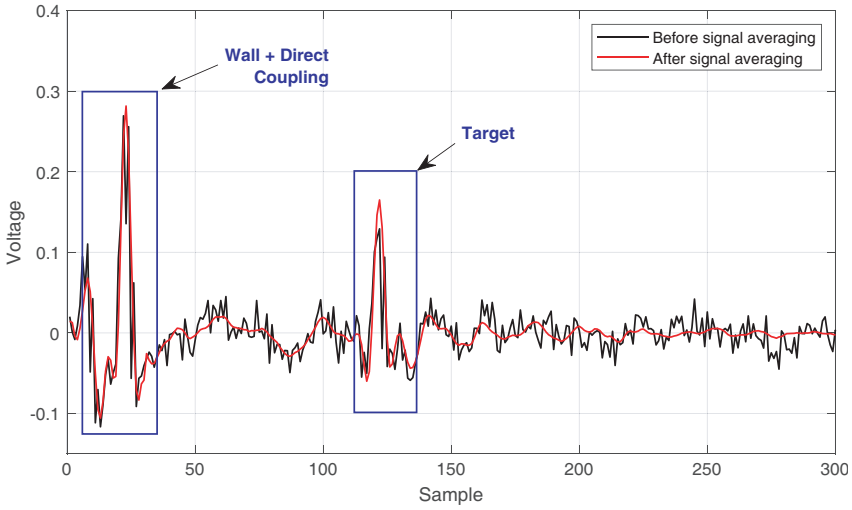

Figure 13. Received signal before and after the signal averaging step.

From the figure, it is clearly shown that the noise oscillation parts are significantly reduced after the signal averaging step, resulting in an improvement in signal-to-noise ratio (SNR) about 5 dB. It is important to note that by increasing the number of PRIs during averaging computation, the radar tends to obtain better results in terms of SNR, but this will slightly increase the time of execution. Using the signal averaging minimizes the impact of the noise signal. However, the reflections due to the wall, as well as the direct coupling between the antennas still exist, which represent the biggest part of the received signal. Hence, background subtraction is applied to reduce these effects, by subtracting the reflected signal in the absence of the target (background signal) from the signal of the wall plus the target responses [34]. As a basic, the background signal represents the scene with no targets. Figure 14(a) shows the background signal plus the target responses and the background signal, and Figure 14(b)

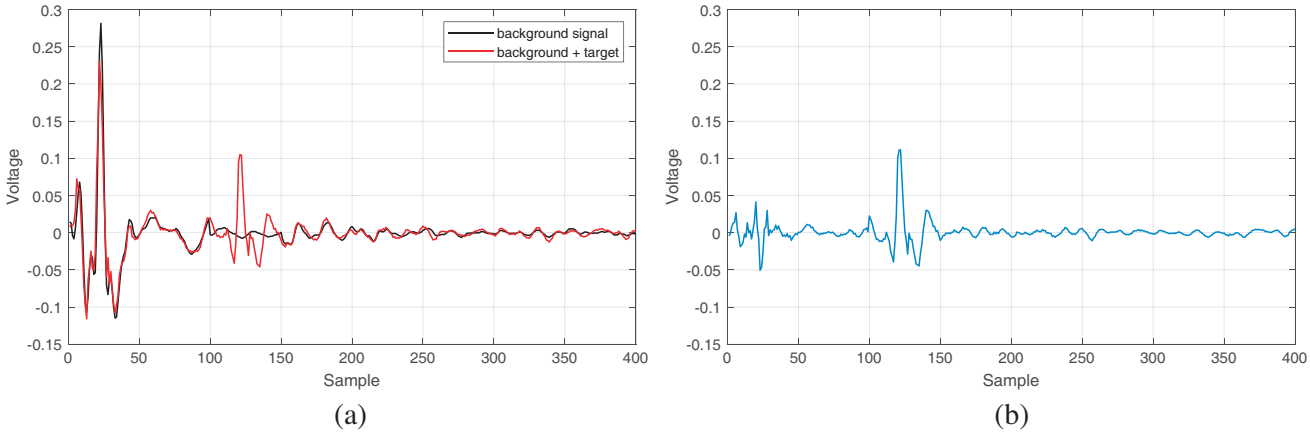

Figure 14. Received signal through the wall, (a) before, (b) after background subtraction.

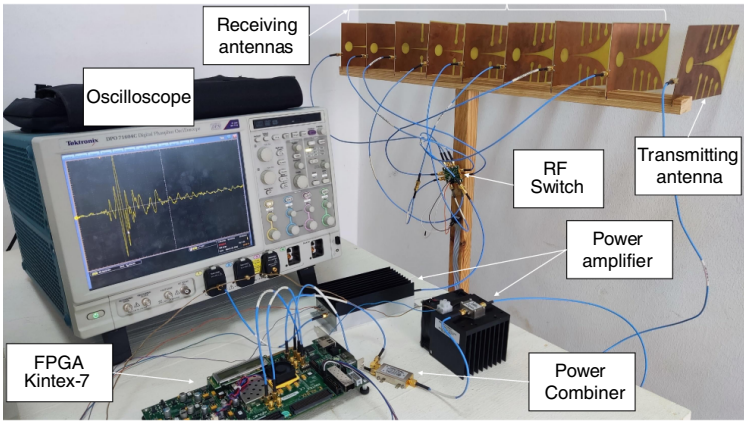

Figure 15. The photography of designed TWI radar structure.

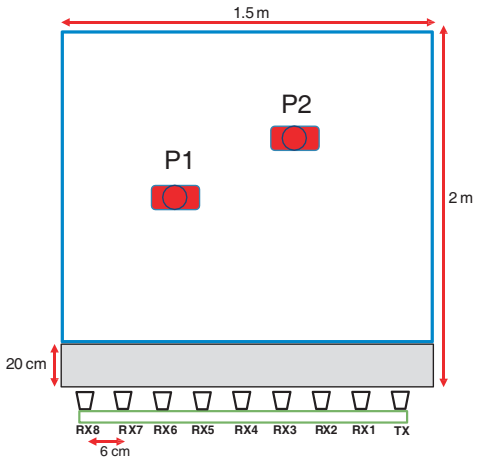

Figure 16. The geometry of illuminated scene.

depicts the received signal through the wall when the background subtraction is carried out. The use of background subtraction significantly minimizes the effect of the wall and direct coupling, as shown in the black plot in Figure 14. Finally, the back-projection algorithm is used to process the collected radar signal to form 2D images of the scene behind a wall.

Through-the-wall imaging experiment was conducted to demonstrate the imaging capability of the designed TWI radar. The imaging scene is composed of two persons standing behind a concrete wall. Figure 15 shows a photograph of the experimental setup that has been developed. The placement of the radar antennas and the location of the human targets are illustrated in Figure 16.

The radar antennas are fixed at a height of 1.5 m in front of a 20 cm thick concrete wall with a dielectric constant of $\varepsilon_r = 8$. The radar uses one transmitting (TX) and eight receiving antennas (RX) spaced at a distance of 6 cm. During the radar experiments, the two human targets stand at positions P1 (0.5 m, 0.8 m) P2 (1 m, 1.2 m) and then at positions P1 (0.5 m, 1.4 m) P2 (1 m, 1 m). Figure 17 plots the experiment results of imaging through the wall. The reconstructed images demonstrate that the developed TWI radar has the potential to produce a high-resolution image of the two human targets and identify their positions.

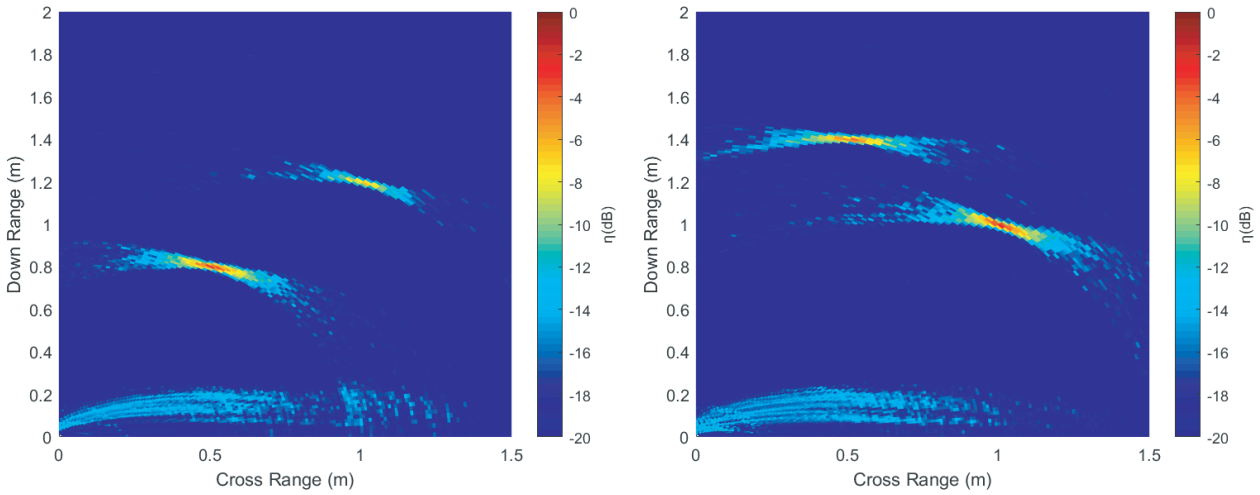

Figure 17. Through-wall-imaging results of two human targets, (a) positions P1 (0.5 m, 0.8 m) P2 (1 m, 1.2 m), (b) P1 (0.5 m, 1.4 m) P2 (1 m, 1 m).

6. COMPARISON WITH RELATED WORKS

In this section, the radar system developed in this paper is compared with recent similar studies in the literature. Table 1 reports the system specifications of the radar discussed in this paper along with previous similar studies. The design of the current radar system relies heavily on advanced FPGA technology, namely the Kintex-7 FPGA board, which offers more functionality and better performance than FPGAs that have been used in previous works. The proposed radar system in this paper provides better range resolution and a wider frequency band, due to the short time duration, wide spectrum, and monocycle shape of the generated impulse UWB signal using the FPGA board. The 400 picoseconds duration of this signal enables the radar to achieve a range resolution of 6 cm, which makes the developed radar system more suitable for multiple target detection and capable of providing high-resolution images. The approach used to produce a UWB signal using the FPGA efficiently generates an impulse UWB signal, which has a monocycle shape and a bandwidth of 4.6 GHz from 0.7 to 5.4 GHz. The spectrum of this monocycle signal is centered directly on the high frequency at 3 GHz. This feature allows

Table 1. Comparison of the proposed IR-UWB radar system with similar study.

	[18]	[19]	[15]	[20]	[21]	Current work
FPGA technology	Virtex-2	Virtex-4	Virtex-4	Virtex-6	Virtex-6	Kintex-7
Application	NA	NA	TWI	TWI	Vital sign	TWI
Pulse shape	NA	NA	Gaussian	Gaussian	Gaussian	Monocycle
Pulse bandwidth	41.5 MHz	90 MHz	1 GHz	1 GHz	2.073 GHz	4.6 GHz
Pulse duration	35 ns	11.55 ns	1 ns	1 ns	540 ps	400 ps
Center frequency	110.25 MHz	300 MHz	3 GHz	3.5 GHz	1 GHz	3 GHz
Frequency band	NA	NA	2.5–3.5 GHz	3–4 GHz	0.1–2.1 GHz	0.7–5.4 GHz
PRF	NA	NA	10 MHz	10 MHz	20 MHz	12 MHz
Range resolution	NA	NA	15 cm	15 cm	8.1 cm	6 cm

simplifying the radar structure by reducing the components required by the radar, such as components needed for signal modulation (e.g., a mixer and local oscillator). On the other hand, the FPGA-based implementation of this UWB generator offers the flexibility to modify the spectrum characteristics, the PRF, and time-duration of the generated signal according to the requirements. This is an attractive solution for the wide application of UWB radar.

7. CONCLUSION

In this paper, we propose an IR-UWB radar system that operates in the frequency band from 0.7 GHz to 5.4 GHz. The FPGA based implementation of the IR-UWB generator allows the production of impulse signals that have good characteristics in terms of signal bandwidth and center frequency. The radar generates a monocycle signal that has a duration of 400 ps and a 4.6-GHz bandwidth. This signal is then used for through-wall imaging of multiple human targets. The experimental result based on the backprojection algorithm demonstrates the imaging resolution of the presented radar system. Moreover, our proposed IR-UWB generator can be easily used to address many other applications, such as vital sign extraction and detection of micro-Doppler signatures.

ACKNOWLEDGMENT

The authors gratefully acknowledge the partial financial support of this research by the Military Polytechnic School of Algeria.

REFERENCES

1. Nkwari, P. K. M., S. Sinha, and H. C. Ferreira, "Through-the-wall radar imaging: A review," *IETE Technical Review*, Vol. 35, No. 6, 631–639, 2017.
2. Verma, P., A. Gaikwad, D. Singh, and M. Nigam, "Analysis of clutter reduction techniques for through wall imaging in UWB range," *Progress In Electromagnetics Research B*, Vol. 17, 29–48, 2009.
3. Wu, Y., F. Shen, D. Xu, and R. Liu, "An ultra-wideband antenna with low dispersion for ground penetrating radar system," *IEEE Sensors Journal*, Vol. 21, No. 13, 15171–15179, 2021.
4. Selvaraj, V., J. B. J. J. Sheela, R. Krishnan, L. Kandasamy, and S. Devarajulu, "Detection of depth of the tumor in microwave imaging using ground penetrating radar algorithm," *Progress In Electromagnetics Research M*, Vol. 96, 191–202, 2020.
5. Song, Y., J. Hu, N. Chu, T. Jin, J. Zhang, and Z. Zhou, "Building layout reconstruction in concealed human target sensing via UWB MIMO through-wall imaging radar," *IEEE Geoscience and Remote Sensing Letters*, Vol. 15, No. 8, 1199–1203, 2018.
6. Zadeh, A. T., M. Diyap, J. Moll, and V. Krozer, "Towards localization and classification of birds and bats in windparks using multiple FMCW-radars at Ka-band," *Progress In Electromagnetics Research M*, Vol. 109, 1–12, 2022.
7. Gao, Z., Y. Jia, S. Liu, and X. Zhang, "Development of ground-based SFCW-ArcSAR system and investigation on point target response," *Progress In Electromagnetics Research M*, Vol. 109, 137–148, 2022.
8. Mahfouz, M., A. Fathy, Y. Yang, E. E. Ali, and A. Badawi, "See-through-wall imaging using ultra wideband pulse systems," *34th Applied Imagery and Pattern Recognition Workshop (AIPR'05)*, Washington, DC, USA, 2005.
9. Wang, Y., Q. Liu, and A. E. Fathy, "CW and pulse-Doppler radar processing based on FPGA for human sensing applications," *IEEE Transactions on Geoscience and Remote Sensing*, Vol. 51, No. 5, 3097–3107, 2012.
10. Crowgey, B. R., E. J. Rothwell, L. C. Kempel, and E. L. Mokole, "Comparison of UWB short-pulse and stepped-frequency radar systems for imaging through barriers," *Progress In Electromagnetics Research*, Vol. 110, 403–419, 2010.

11. Yang, D., Z. Zhu, J. Zhang, and B. Liang, "The overview of human localization and vital sign signal measurement using handheld IR-UWB through-wall radar," *Sensors*, Vol. 21, No. 2, 402, 2021.
12. Sadoudi, S., M. S. Azzaz, M. Djeddou, and M. Benssalah, "An FPGA real-time implementation of the Chen's chaotic system for securing chaotic communications," *International Journal of Nonlinear Science*, Vol. 7, No. 4, 467–474, 2009.
13. Lee, Y. C., Y. K. Chan, and V. Koo, "Design and implementation of field-programmable gate array based fast Fourier transform co-processor using verilog hardware description language," *Progress In Electromagnetics Research B*, Vol. 92, 47–70, 2021.
14. Sharma, R., O. Yurduseven, B. Deka, and V. Fusco, "Hardware enabled acceleration of near-field coded aperture radar physical model for millimetre-wave computational imaging," *Progress In Electromagnetics Research B*, Vol. 90, 91–108, 2021.
15. Yang, Y. and A. E. Fathy, "Development and implementation of a real-time see-through-wall radar system based on FPGA," *IEEE Transactions on Geoscience and Remote Sensing*, Vol. 47, No. 5, 1270–1280, 2009.
16. Chua, M. Y. and V. C. Koo, "FPGA-based chirp generator for high resolution UAV SAR," *Progress In Electromagnetics Research*, Vol. 99, 71–88, 2009.
17. Firmansyah, I. and Y. Yamaguchi, "FPGA-based implementation of a chirp signal generator using an OpenCL design," *Microprocessors and Microsystems*, Vol. 77, 103199, 2020.
18. Park, Y. and D. D. Wentzloff, "All-digital synthesizable UWB transmitter architectures," *IEEE International Conference on Ultra-Wideband*, Vol. 2, 29–32, 2008.
19. Duraiswamy, P., X. Li, J. Bauwelinck, J. Vandewege, P. Vaes, and S. Teughels, "Synchronous delay based UWB pulse generator in FPGA," *IEICE Electronics Express*, Vol. 9, No. 9, 868–873, 2012.
20. Saad, M., A. Maali, M. S. Azzaz, and I. Kakouche, "An experimental platform of impulse UWB radar for through-wall imaging based on FPGAs," *International Conference on Communications Control Systems and Signal Processing*, 198–201, 2020.
21. Tantiparimongkol, L. and P. Phasukkit, "IR-UWB pulse generation using FPGA scheme for through obstacle human detection," *Sensors*, Vol. 20, No. 13, 3750, 2020.
22. Hu, B. and N. C. Beaulieu, "Pulse shapes for ultrawideband communication systems," *IEEE Transactions on Wireless Communications*, Vol. 4, No. 4, 1789–1797, 2005.
23. Chen, X. and S. Kiaei, "Monocycle shapes for ultra wideband system," *2002 IEEE International Symposium on Circuits and Systems (ISCAS)*, Phoenix-Scottsdale, AZ, USA, 2002.
24. Skolnik, M. I., *Radar Handbook*, McGraw-Hill, New York, 1970.
25. Cui, G., L. Kong, and J. Yang, "A back-projection algorithm to stepped-frequency synthetic aperture through-the-wall radar imaging," *IEEE 1st Asian and Pacific Conference on Synthetic Aperture Radar, APSAR 2007*, 123–126, 2007.
26. Soumekh, M., *Synthetic Aperture Radar Signal Processing with Matlab Algorithms*, Wiley, New York, NY, 1999.
27. Barrie, G., "Ultra-wideband synthetic aperture imaging: Data and image processing," *Defence RD Canada-Ottawa*, Ottawa, 2003.
28. Jin, T., B. Chen, and Z. Zhou, "Image-domain estimation of wall parameters for autofocusing of through-the-wall SAR imagery," *IEEE Transactions on Geoscience and Remote Sensing*, Vol. 51, No. 3, 1836–1843, 2012.
29. Ahmad, F., Y. Zhang, and M. G. Amin, "Three-dimensional wideband beamforming for imaging through a single wall," *IEEE Geoscience and Remote Sensing Letters*, Vol. 5, 176–179, 2008.
30. X. Inc., *7 series FPGAs GTX/GTH transceivers user guide*, Xilinx, 2015.
31. X. Inc., *Kintex-7 FPGA KC705 Evaluation Kit*, Xilinx, 2012.
32. Tahar, Z., X. Derobert, and M. Benslama, "An ultra-wideband modified vivaldi antenna applied to through the ground and wall imaging," *Progress In Electromagnetics Research B*, Vol. 86, 111–122, 2018.

33. Wang, Y. and A. E. Fathy, "Advanced system level simulation platform for three-dimensional UWB through-wall imaging SAR using time-domain approach," *IEEE Transactions on Geoscience and Remote Sensing*, Vol. 50, No. 5, 1986–2000, 2011.
34. Dehmollaian, M., M. Thiel, and K. Sarabandi, "Through-the-wall imaging using differential SAR," *IEEE Transactions on Geoscience and Remote Sensing*, Vol. 47, No. 5, 1289–1296, 2009.